

Reduction of Suspended Graphene Oxide Single Sheet Nanopaper: The Effect of Crumpling

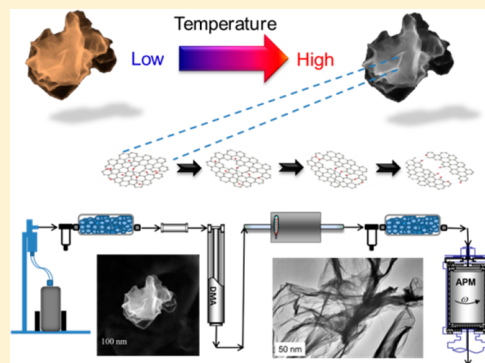
Xiaofei Ma,^{†,‡} Michael R. Zachariah,^{†,‡} and Christopher D. Zangmeister^{*,†}

[†]Material Measurement Laboratory, National Institute of Standards and Technology, Gaithersburg, Maryland 20899, United States

[‡]Department of Mechanical Engineering and Department of Chemistry and Biochemistry, University of Maryland, College Park, Maryland 20742, United States

S Supporting Information

ABSTRACT: The recent development of aerosol generated crumpled graphene oxide nanopaper provides a test bed for studying the reactivity of physically deformed graphene-based materials. In this work, we measured the thermal reduction of aerosolized single sheet, crumpled graphene oxide (GO) nanopaper. Online aerosol mass analysis was used to monitor the mass evolution of individual crumpled GO nanopaper during reduction. For the first time, the extent of sp^2 bonding within the material was characterized using photoacoustic spectroscopy. The chemical composition of reduced GO nanopaper was evaluated using X-ray photoemission spectroscopy (XPS). Thermal reduction kinetics was determined using both the loss of mass and the change in optical absorption, each measured as a function of temperature. The activation energies were different for the two techniques, suggesting mass loss and light absorption probe different processes of GO reduction. We measured a constant effective density at high reduction temperatures suggesting that portions of reduced GO unzip from the sheet similar to what has been observed in oxidized graphene.



INTRODUCTION

Graphene oxide (GO) is a water-soluble electronic hybrid material, featuring both sp^2 and sp^3 carbon environments with various oxygen containing functional groups. Through reduction, the disrupted sp^2 network of GO can be partially restored, making GO a solution processable precursor to graphene-like materials. The availability of different oxygen functional groups and the variety of chemical interactions between these functional groups and other materials allows synthesis of hybrid materials¹ and composites from GO.² Its heterogeneous atomic and electronic structure has led to novel optoelectronic properties when compared to graphene.³ Furthermore, the properties of GO can be tuned through careful and controlled removal of specific oxygen moieties, which has opened a wide range of applications.^{4–8}

Various chemical and thermal methods have been developed to reduce GO to a graphene-like material (rGO). Most chemical methods involve the use of strong chemical reductants,^{9–12} while thermal treatment, avoiding the use of hazardous chemicals, also provides an efficient method for GO reduction.¹³ During reduction, the restoration of the sp^2 network and the decrease in oxygen functionality has been observed, accompanied by the evolution of H_2O , CO_2 , and CO gases. High-resolution TEM has revealed that thermal reduction forms graphene-like areas that are interspersed with defect regions dominated by clustered carbon pentagon and heptagon rings,¹⁴ holes (up to 5 nm^2), and remaining oxygen containing functionalities,¹⁵ adding strain and distortion in the

defected regions. Control of reduced GO properties requires understanding the reduction process, which, due to its complexity and the lack of a detailed reaction mechanism, prevents the accurate prediction of rGO properties. Furthermore, these properties are functions of the size, shape, chemical composition, and ratio of the sp^2 and sp^3 fractions of the starting material, which are highly varied depending on the synthetic scheme.

One phenomenon of graphene-based materials is how the chemical reactivity is affected by its morphology.¹⁶ Recent developments using aerosol generation to form highly folded, crumpled single sheet GO nanopapers (similar in morphology to macroscopic crumpled paper) at high concentration ($>10^6$ particles cm^{-3}) allows fundamental properties to be studied in the absence of substrate and/or mass and heat transfer effects.^{17–19} First, crumpled GO nanopaper can be used to assess if morphology is related to chemical reactivity. GO nanopapers are highly crumpled and comprise multiple ridges and wrinkles leading to regions of high strain and energy densities, which allow the effect of particle morphology to be measured relative to planar GO properties. Theoretical work has predicted enhanced chemical activity of the atoms along the kinks and ridges in GO.²⁰ Second, GO crumpled nanopaper consists of single GO sheets; thus, effects such as intercalated

Received: January 8, 2013

Revised: January 17, 2013

Published: January 18, 2013

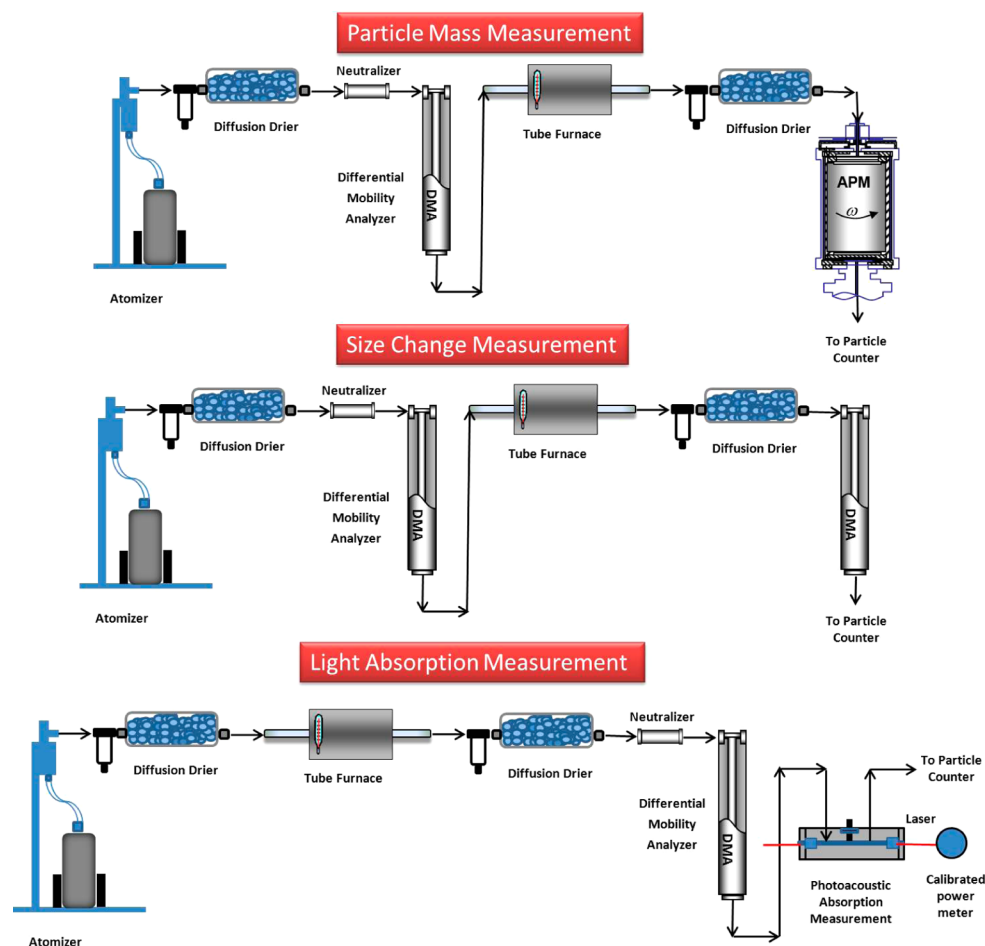


Figure 1. Experimental schematic.

water driven hole and carbonyl formation are minimized.²¹ Finally, aerosolized crumpled GO is unsupported in a flowing gas stream, where GO can achieve its most thermodynamically favorable state without effects from substrate interaction. To date, prior studies have measured thermochemical properties of GO single and multilayered films, where there may be influence from the substrate. It is well established that adsorption of gases, monomolecular films, and some thin layers can greatly affect adsorbate properties such as bond strength, electron density, and extent and direction of charge transfer. These effects are minimized in this study.

We demonstrate a method to quickly reduce freely suspended GO nanopaper to rGO using an aerosol reactor and measure activation energies associated with the reduction process. The reaction kinetics was determined by nanoparticle mass analysis, as well as optical absorption using photoacoustic spectroscopy. Mass measurements of individual GO particles provide a direct measure of desorption of functional groups and H₂O. Optical absorption probes the sp² network, which both theoretical and experimental work²² have shown that the extent of sp² islands governs the optical and electronic properties of carbonaceous materials.²³ The data are compared to previous thermal reduction studies of planar GO films on solid surfaces.

EXPERIMENTAL SECTION

GO Preparation. GO was synthesized using a modified version of the Hummer's method as described previously.^{13,24} Dried GO powder was added to 18.2 MΩ cm H₂O at 0.5 mg/

mL. The GO concentration was determined from UV–vis absorption measurement at 400 nm. XPS results shows the initial C/O of GO is near 2.

DMA-APM and Tandem DMA Systems. A schematic of the instrumental set up employed is shown in Figure 1. All experiments were carried out in air (21% O₂) unless otherwise noted. The mass and size evolution of GO nanopaper under different reduction conditions were measured by combining two ion-mobility measurements in series. The first selects the mobility diameter of GO particles with a differential mobility analyzer (DMA), and the second employs either an aerosol particle mass analyzer (APM) or a second DMA, to measure the mass or size change of GO nanopaper resulting from a controlled reduction environment. The details of the system configuration and error analysis have been described previously.^{25–28} The commercially available DMA and APM instruments are combined and coupled to a condensation particle counter (CPC). The reported particle mass was determined by fitting the data to a Gaussian line shape to a particle count versus mass plot at each mobility diameter. The DMA-APM mass measurement was calibrated with NIST Standard Reference Materials (SRM) PSL spheres of 100.7 nm (SRM 1963A) and 310 nm (SRM 1961). The mass measurement error is within 3.5% for 310 nm PSL and 2.8% for 100.7 nm PSL. Run to run error is within 0.2% for 310 nm PSL and 0.14% for 100.7 nm PSL spheres. GO reduction was performed in a quartz flow tube. The temperature in the flow tube was monitored with a NIST calibrated type K

thermocouple. Aerosol flow rates were controlled by carefully adjusting the ratio of flow through the quartz tube versus a HEPA filter assembly. The flow rate was monitored using a calibrated flow monitor in line with the flow tube. In the experiment, the flow rate through the system is kept at 1.5 L per minute (lpm), which gives a ~ 5 s residence time in the reduction furnace.

The effective density is calculated by dividing the measured GO mass by the equivalent spherical volume ($4/3\pi r^3$, where r is the mobility radius) from the particle size measurement. Our previous density measurement of NIST standard reference (SRM) spheres using the same DMA-APM configuration showed an uncertainty within 4% and run to run consistency within 0.2%.²⁹

X-ray Photoemission Spectroscopy (XPS). Particle samples for XPS analysis were collected from aerosol phase onto an Al substrate using an electrostatic particle collector. XPS measurements were made on a commercially available multichannel X-ray photoemission spectrometer using a monochromatic Al K α source and a 40 eV pass energy. Data was fit as described in ref 13.

Photoacoustic Spectroscopy. The photoacoustic spectrometer consists of an acoustic cell, a microphone, a 300 mW continuous-wave laser at $\lambda = 660$ nm, a lock-in amplifier, a calibrated laser power meter, and a data acquisition system. Details and error analysis of the system is described in Gillis et al.³⁰ and Havey et al.,³¹ and a schematic is shown in Figure 1. The photoacoustic spectrometer (PAS) measures the absorption of the total population of size-selected particles. The absorption cross-section per particle is then obtained by dividing the PAS absorption cross-section by the aerosol concentration downstream measured using a condensation particle counter (CPC). The particle loss inside the PAS chamber is independent of particle size. Finally, the mass absorption cross-section was calculated by dividing the absorption cross-section per particle by the particle mass.

SEM and TEM. Transmission (TEM) and scanning electron microscopy (SEM) measurements were made on a commercially available instrument. GO thin films were drop cast onto SiO₂ substrates and dried in a vacuum desiccator and heated in an oven in laboratory air. GO nanopaper particles were collected on TEM grids using an electrostatic particle collector.

RESULTS AND DISCUSSION

Our previous work showed aerosolization of GO aqueous solution and rapid solvent removal crumples 2-dimensional GO nanosheets by capillary forces where the final morphology is identical in shape and fractal dimension to that of macroscopic crumpled paper.¹⁷ The particle morphology can be envisioned as consisting of a 2-dimensional sheet crumpled into 3-dimensional space, where gas evolution (via reduction) and heat transfer are equally accessible to all regions of the particle. The aerosolization method produces freely suspended GO nanopapers with a particle size distribution from 100 to 400 nm which peaks around 150 nm. A typical SEM image of crumpled nanopaper with a 150 nm mobility diameter is shown in the inset of Figure 2. The mass of 150 nm mobility diameter GO is 1.5 ± 0.1 femtograms, corresponding to an effective density of 0.95 g/cm^3 , consistent with single sheet particles with an open, crumpled morphology.

Figure 2 shows the results of particle mass, size (measured by tandem DMA), and effective density of size selected 150 nm GO crumpled nanopaper as a function of reduction temper-

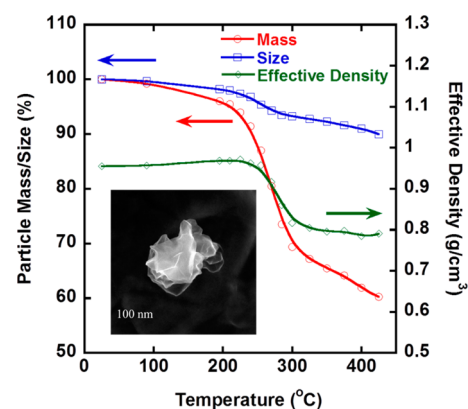


Figure 2. Mass, size, and effective density evolutions of 150 nm size-selected GO crumpled nanopaper reduction; inset, SEM image of crumpled GO nanopaper.

ature in air (21% O₂). Three mass loss regions can be identified. The first region comprises about 5% of the total mass and starts around 100 °C, which is correlated with the loss of residual H₂O and loosely bonded functional groups.³² The largest mass loss, with an onset temperature of about 225 °C, is sharp and results in the loss of an additional 25% of the total mass. The third mass loss region has a reduced slope, starts 300 to 325 °C, and continues to 425 °C, contributing to about 10% of particle mass loss. The rapid mobility diameter change occurring between 225 and 300 °C is correlated with measured mass loss. Combining the mass and mobility diameter data, the effective density measurement shows a $\sim 20\%$ decrease between 225 and 300 °C, while almost constant density is observed at both lower and higher temperatures. Our previous measurement of the fractal dimension of aerosolized GO showed that the shape of GO nanopaper is invariant at temperatures >400 °C.¹⁷ The loss of mass occurs homogeneously to maintain constant density, while preserving the overall morphology at a given mobility diameter. Therefore, the effective density decrease of GO nanopaper between 225 and 300 °C captures the GO to rGO transition.

The effect of carrier gas on the mass loss of GO nanopaper was also investigated. Mass loss of 150 nm GO nanopaper in air and Ar are shown in Figure 3. GO mass loss is nearly identical for temperatures <425 °C, above which we observe mass loss is

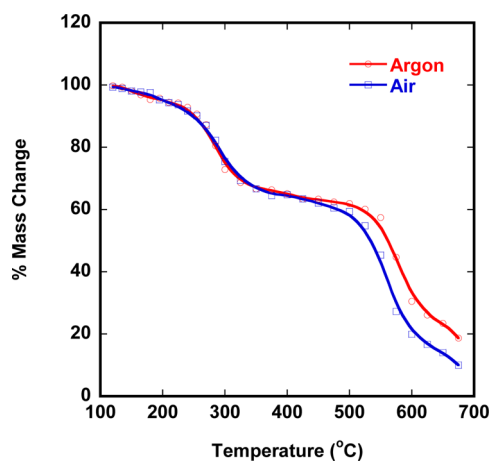


Figure 3. Mass change of size selected 150 nm GO nanopaper as a function of temperature in air (21% O₂) and Ar.

about 5% higher in air. This is likely the result of the presence of O₂ in air, although we cannot rule out a small amount of O₂ in Ar. While GO thermal reduction at 400 °C in Ar has been previously demonstrated, a partial pressure 10^{-5} Torr of O₂ can result in complete loss of planar single layer GO,³² and O₂ induced mass loss may be exacerbated in crumpled nanosheets with exposed edges in a flowing gas stream.

Optical absorption of GO nanopaper aerosol as a function of temperature is shown in Figure 4. The GO mass absorption

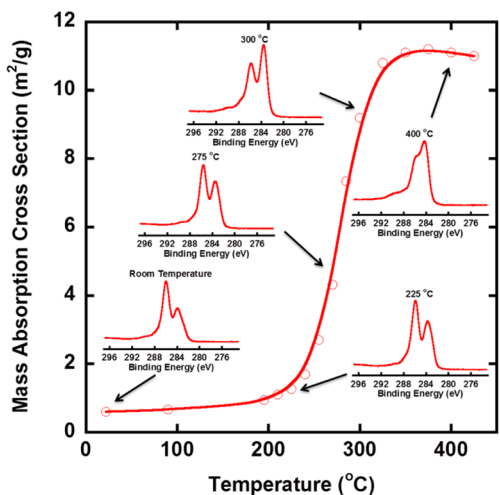


Figure 4. Mass absorption cross-section of size-selected 150 nm GO as a function of reduction temperature. XPS data show the C 1s region for each corresponding temperature.

efficiency (MAE, m²/g) is constant until ~200 °C, where a rapid increase in MAE is initiated and continues to 325 °C. Above this temperature, the GO optical absorption becomes constant, correlating with the effective density. The optical absorption curve suggests that there is little improvement in the restoration of the sp² network above 325 °C at the reduction time scale of our experiment, although the particle mass continues decreasing. C 1s core level XPS of GO aerosol were

collected as a function of temperature and also are shown in Figure 4. The full XPS elemental analysis shows the presence of only carbon and oxygen. Prior to thermal processing, three peaks are resolved in the C 1s region; one at 284.6 eV attributed to C–C bonds and two peaks at higher binding energies are assigned to carbon bonded to oxygen (peak fits and peak component ratios are shown in the Figure S1 and Table S1, Supporting Information, respectively). During thermal reduction, a continuous shift of the components to lower binding energy is observed with increasing reduction temperature, indicating a loss of carbon bound to oxygen with concomitant increase in the C–C component. The C 1s XPS spectrum at 400 °C shows the increase in the component at 284.6 eV, typical of thermal reduction and increase in sp² bonding. The collected aerosol color changed from light brown to dark brown to black as the temperature was increased, consistent with both the formation of new sp² bonds and with our optical measurements.²³

Figure 5a shows TEM images of mobility diameter selected 150 nm GO particles heated during image acquisition at room temperature and at 480 °C in vacuum. The most obvious changes occur at the periphery ridges and folded areas, where well-defined ridges and wrinkles at room temperature are slightly offset in space and replaced by more rounded regions and disappearance of the sharp edges (see arrows), suggesting the edge regions are more reactive than the nanosheet interior regions and consistent with other work.¹⁶ The overall shape (mobility diameter) of the GO particle is preserved, consistent with measurements showing that the fractal dimension of GO particles is independent of temperature.¹⁷

GO nanopaper undergoes fast reduction between 225 and 300 °C. Above 325 °C, little change is observed, as evaluated using both optical absorption and XPS measurements. This is likely a result of the remnants of stable ether and carbonyl groups on the nanosheet.³³ The continuous mass decrease and constant particle density are consistent with cleavage and mass loss of GO fragments at ≥325 °C, most likely from these highly reactive folded areas. As discussed above, we measured mass loss in air (21% O₂) and Ar, and the measured mass loss at

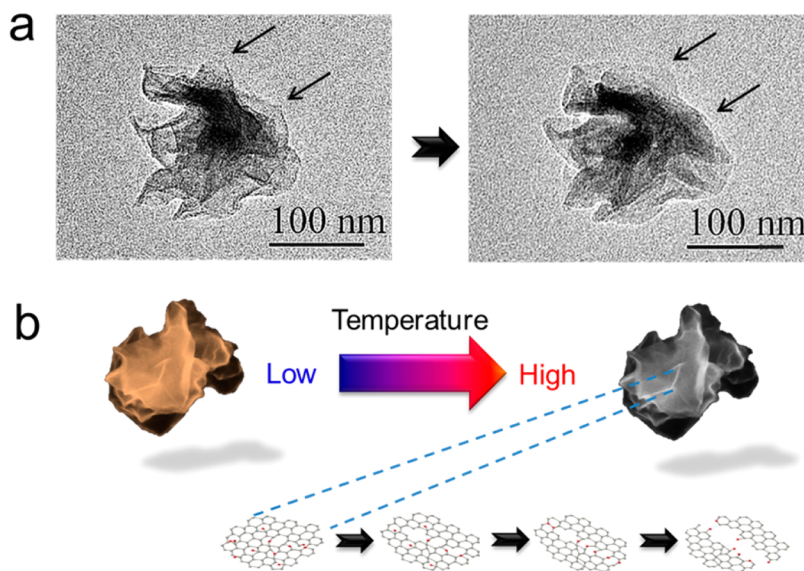


Figure 5. (a) TEM in situ heating experiment of a 150 nm GO from room temperature (left) to 480 °C (right) (TEM images are reproduced from our previous work; see ref 17). (b) Schematic of GO nanopaper mass loss mechanism at high temperatures.

temperatures <425 °C are within our mass loss uncertainty. This suggests that pyrolysis or mass loss associated with etching of the edges with O₂ is unlikely at low temperatures. A proposed mechanism of high temperature mass loss is presented in Figure 5b. During the reduction process, holes and defects are generated as mass is lost as CO₂ and H₂O. Studies of GO thermal reduction^{14,15} have shown that, upon heating, holes and defects enlarge, producing significant in-plane distortion and strain within the defect and migrate to form a continuous defect region, and initiate GO fragment cleavage and relax strain at constant density. This mechanism is analogous to an oxygen-induced fragment unzipping in other carbonaceous materials such as oxidized graphene^{34–36} and carbon nanotubes.³⁷ DFT calculations have also predicted the unzipping of oxidized graphene, which has similar chemical composition to GO and partially reduced GO.^{38–41}

The kinetics of GO thermal reduction as a function of reaction time was determined from both mass loss and optical measurements and allowed comparison to the reduction of 2-dimensional GO films. Mass loss probes the evolution of products formed during thermal reduction, whereas the change to the optical cross-section measures the rate of sp² bond formation within the nanosheet. This is achieved by carefully varying the aerosol flow rate through the reduction furnace. The results are displayed in Figure 6. Three temperatures were

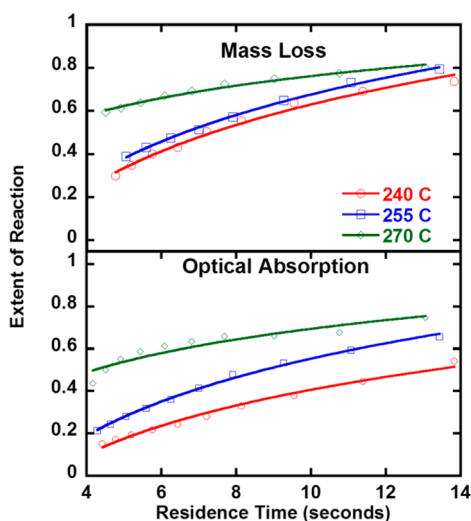


Figure 6. Extent of reduction as a function of residence time for mass and optical absorption measurements at 240, 255, and 270 °C.

used along the thermal reduction region (240, 255, and 270 °C) with the highest rate of mass and optical change. The experimental curves were fit separately and evaluated to determine the relevant kinetic model⁴² as described in ref 42, and the uncertainty was determined by calculating the standard error in the slope of Arrhenius plot. The general reaction rate equation can be written as

$$\frac{d\alpha}{dt} = k(T)f(\alpha)$$

where α is the extent of reaction, $k(T)$ is the temperature-dependent rate constant, and $f(\alpha)$ is the reaction model. The best fit was accomplished with a second-order reaction model ($f(\alpha) = (1-\alpha)^2$, $g(\alpha) = [1/(1-\alpha)] - 1$) for both the mass change and optical absorption data, consistent with the previous results of GO thermal reduction.⁴³ With the reaction

model, the corresponding rate constants at each temperature for an aerosol flow of 1.5 lpm were obtained. The rate constants are plotted in Arrhenius form as shown in Figure 7, and

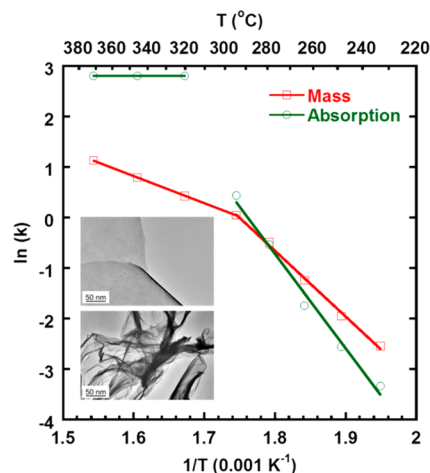


Figure 7. Arrhenius plot of GO reduction rate. The activation energies from mass data are 25.8 ± 0.8 and 10.7 ± 0.1 kcal mol⁻¹ for 200 to 300 °C and at >325 °C, respectively. The activation energy from the optical absorption between 200 to 300 °C is 37.2 ± 2.4 kcal mol⁻¹, and 0 above 325 °C, suggesting no reaction takes place. Inset upper image, GO thin film from dropcast, comprising multiple layers of sheets slowly dried at room temperature; inset lower image, GO thin film from dropcast slowly dried at room temperature and heated at 250 °C for 3 min.

activation energies for each reaction region were determined by linear fits of the reaction rates. Using the mass change data, activation energies of 25.8 ± 0.8 kcal mol⁻¹ and 10.7 ± 0.1 kcal mol⁻¹ are obtained for 200 to 300 °C and at >325 °C, respectively, and are tabulated in Table 1. The activation energy

Table 1. Measured Mass Loss and Optical GO Thermal Reduction Activation Energies in Each Temperature Range

temperature range (°C)	measured activation energy (kcal/mol)	
	mass loss	optical
225 to 300	25.8 ± 0.8	37.2 ± 2.4
>300	10.7 ± 0.1	

from the optical absorption between 200 to 300 °C was of 37.2 ± 2.4 kcal mol⁻¹. The observation of two activation energies shows that the mass loss is not directly correlated and with sp² formation in the 200 to 300 °C reduction regime. Mass loss of GO is observed starting at ~20 °C lower than the absorption cross-section onset temperature. At temperatures >325 °C, the mass loss suggests that the mechanism changes from thermal reduction to the cleavage of fragments from the sheet, as previously discussed. The measured activation energy in this region (10.7 ± 0.1 kcal mol⁻¹) is also similar to the unzipping of graphene fragments upon oxidation (11.5 kcal mol⁻¹).³⁸ The constant effective density at >325 °C coupled with lowered activation energy suggests that this temperature region can be attributed to the migration of defects, also recently observed in rGO using high-resolution TEM.¹⁵ Since crumpled GO nanosheets have relatively higher percentage of its area comprising reactive edges, it is plausible this results in a reduced activation energy.

Previous reports of resistivity measurements of single-layer GO reduction on a solid surface⁴³ measured an activation energy of 37 kcal mol⁻¹, which is within uncertainty of our activation energy obtained using optical absorption as expected since both techniques probe sp² bonding within the nanosheet and are independent of particle morphology. The kinetics of GO reduction using the loss of CO₂ and H₂O as a function of temperature from planar thin GO films measured the activation energy as 32 kcal mol⁻¹. Activation barriers obtained from gravimetric analysis on multilayered planar GO films⁴⁴ fall within resistivity and mass loss measurements (32 to 38 kcal mol⁻¹). In addition to potential interaction of GO films with substrate, the interpretation of thermal reduction of multilayer and thin GO films is complicated by the loss of interstitial H₂O at 130 °C in addition to the mass loss associated with thermal reduction between 220 and 250 °C. Although measured activation energy from mass loss in our experiments is ~7 to 12 kcal mol⁻¹ lower than results of both multi- and monolayer planar GO films adsorbed on a surface, it is unlikely that factors such as interstitial H₂O loss is a contributor in our experiment as the aerosolization process forms single GO sheets. The morphology of crumpled GO particles is highly open when compared to a multilayer GO film that has layer GO spacing of ~0.7 nm. In multilayered GO films, the layers are hydrogen bonded by H₂O and van der Waals forces.^{21,45} Thus, crumpled GO can be modeled as a single sheet, as there is little chemical interaction (hydrogen bonding) between neighboring folds and ridges. The differences in activation energy values highlight the potential of enhanced reactivity at the folded and ridge areas present in crumpled GO nanopaper relative to 2-dimensional planar GO films, and the sp² bond formation is independent of morphology. The precrumpled nanosheets may reduce the mass loss activation barrier when compared to planar GO films as they contain more reactive folds and ridges and more edge regions. TEM images of drop cast GO thin films, see Figure 7 inset, show that crumpling is a thermodynamically favored process induced during the thermal reduction process. The observation of GO crumpling or folding in heated GO thin films has been observed in studies and a crumpled morphology may be the most thermodynamically favorable state of rGO, relieving strain within the film upon the mass loss associated with reduction.^{46–49} Thus, the larger activation energies measured for GO thin films may be the combination of thin film crumpling and thermal reduction. Crumpling can be envisioned as an additional activation barrier requiring energy to initiate the morphological change from a planar sheet.

CONCLUSIONS

In summary, we have measured the thermal reduction of GO using a combination of size, mass, and optical properties as a function of temperature. Our data shows that GO reduction occurs as the loss of mass and the formation of new sp² bonds. However, the temperature dependencies of mass loss and bond formation show that GO thermal reduction occurs at different reaction rates. The formation of high energy edges and ridges induced during the GO nanopaper crumpling process is likely an important contributor to the overall reduction of GO thin films.

ASSOCIATED CONTENT

Supporting Information

XPS data of 150 nm GO aerosol at 22 °C and a typical spectra were fit with three components; Table of XPS components.

This material is available free of charge via the Internet at <http://pubs.acs.org>.

AUTHOR INFORMATION

Corresponding Author

*E-mail: christopher.zangmeister@nist.gov.

Notes

The authors declare no competing financial interest.

ACKNOWLEDGMENTS

We would like to acknowledge the technical insight and aid received from Drs. Wen-An Chiou and Li-Chung Lai, The Maryland Nanocenter, and the Nanoscale Imaging Spectroscopy and Properties (NISP) Laboratory at the University of Maryland.

REFERENCES

- (1) Wang, H. L.; Cui, L. F.; Yang, Y. A.; Casalongue, H. S.; Robinson, J. T.; Liang, Y. Y.; Cui, Y.; Dai, H. J. Mn₃O₄-Graphene Hybrid as a High-Capacity Anode Material for Lithium Ion Batteries. *J. Am. Chem. Soc.* **2010**, *132*, 13978–13980.
- (2) Stankovich, S.; Dikin, D. A.; Dommett, G. H. B.; Kohlhaas, K. M.; Zimney, E. J.; Stach, E. A.; Piner, R. D.; Nguyen, S. T.; Ruoff, R. S. Graphene-Based Composite Materials. *Nature* **2006**, *442*, 282–286.
- (3) Loh, K. P.; Bao, Q.; Eda, G.; Chhowalla, M. Graphene Oxide As a Chemically Tunable Platform for Optical Applications. *Nat. Chem.* **2010**, *2*, 1015–1024.
- (4) Robinson, J. T.; Perkins, F. K.; Snow, E. S.; Wei, Z. Q.; Sheehan, P. E. Reduced Graphene Oxide Molecular Sensors. *Nano Lett.* **2008**, *8*, 3137–3140.
- (5) Eda, G.; Chhowalla, M. Chemically Derived Graphene Oxide: Towards Large-Area Thin-Film Electronics and Optoelectronics. *Adv. Mater.* **2010**, *22*, 2392–2415.
- (6) Wang, X.; Zhi, L. J.; Mullen, K. Transparent, Conductive Graphene Electrodes for Dye-Sensitized Solar Cells. *Nano Lett.* **2008**, *8*, 323–327.
- (7) Kamat, P. V. Graphene-Based Nanoassemblies for Energy Conversion. *J. Phys. Chem. Lett.* **2011**, *2*, 242–251.
- (8) Ng, Y. H.; Lightcap, I. V.; Goodwin, K.; Matsumura, M.; Kamat, P. V. To What Extent Do Graphene Scaffolds Improve the Photovoltaic and Photocatalytic Response of TiO₂ Nanostructured Films? *J. Phys. Chem. Lett.* **2010**, *1*, 2222–2227.
- (9) Stankovich, S.; Dikin, D. A.; Piner, R. D.; Kohlhaas, K. A.; Kleinhammes, A.; Jia, Y.; Wu, Y.; Nguyen, S. T.; Ruoff, R. S. Synthesis of Graphene-Based Nanosheets via Chemical Reduction of Exfoliated Graphite Oxide. *Carbon* **2007**, *45*, 1558–1565.
- (10) Shin, H.-J.; Kim, K. K.; Benayad, A.; Yoon, S.-M.; Park, H. K.; Jung, I.-S.; Jin, M. H.; Jeong, H.-K.; Kim, J. M.; Choi, J.-Y.; Lee, Y. H. Efficient Reduction of Graphite Oxide by Sodium Borohydride and Its Effect on Electrical Conductance. *Adv. Funct. Mater.* **2009**, *19*, 1987–1992.
- (11) Gilje, S.; Han, S.; Wang, M.; Wang, K. L.; Kaner, R. B. A Chemical Route to Graphene for Device Applications. *Nano Lett.* **2007**, *7*, 3394–3398.
- (12) Gao, X.; Jang, J.; Nagase, S. Hydrazine and Thermal Reduction of Graphene Oxide: Reaction Mechanisms, Product Structures, and Reaction Design. *J. Phys. Chem. C* **2010**, *114*, 832–842.
- (13) Zangmeister, C. D. Preparation and Evaluation of Graphite Oxide Reduced at 220 °C. *Chem. Mater.* **2010**, *22*, 5625–5629.
- (14) Gomez-Navarro, C.; Meyer, J. C.; Sundaram, R. S.; Chuvilin, A.; Kurasch, S.; Burghard, M.; Kern, K.; Kaiser, U. Atomic Structure of Reduced Graphene Oxide. *Nano Lett.* **2010**, *10*, 1144–1148.
- (15) Erickson, K.; Erni, R.; Lee, Z.; Alem, N.; Gannett, W.; Zettl, A. Determination of the Local Chemical Structure of Graphene Oxide and Reduced Graphene Oxide. *Adv. Mater.* **2010**, *22*, 4467–4472.
- (16) Ruoff, R. A Means to an End. *Nature* **2012**, *483*, S42–S42.

- (17) Ma, X. F.; Zachariah, M. R.; Zangmeister, C. D. Crumpled Nanopaper from Graphene Oxide. *Nano Lett.* **2012**, *12*, 486–489.
- (18) Chen, Y.; Guo, F.; Jachak, A.; Kim, S.-P.; Datta, D.; Liu, J.; Kulaots, I.; Vaslet, C.; Jang, H. D.; Huang, J.; Kane, A.; Shenoy, V. B.; Hurt, R. H. Aerosol Synthesis of Cargo-Filled Graphene Nanosacks. *Nano Lett.* **2012**, *12*, 1996–2002.
- (19) Mao, S.; Wen, Z.; Kim, H.; Lu, G.; Hurley, P.; Chen, J. A General Approach to One-Pot Fabrication of Crumpled Graphene-Based Nanohybrids for Energy Applications. *ACS Nano* **2012**, *6*, 7505–7513.
- (20) Srivastava, D.; Brenner, D. W.; Schall, J. D.; Ausman, K. D.; Yu, M. F.; Ruoff, R. S. Predictions of Enhanced Chemical Reactivity at Regions of Local Conformational Strain on Carbon Nanotubes: Kinky Chemistry. *J. Phys. Chem. B* **1999**, *103*, 4330–4337.
- (21) Acik, M.; Mattevi, C.; Gong, C.; Lee, G.; Cho, K.; Chhowalla, M.; Chabal, Y. J. The Role of Intercalated Water in Multilayered Graphene Oxide. *ACS Nano* **2010**, *4*, 5861–5868.
- (22) Chhowalla, M.; Ferrari, A. C.; Robertson, J.; Amaratunga, G. A. J. Evolution of sp(2) Bonding with Deposition Temperature in Tetrahedral Amorphous Carbon Studied by Raman Spectroscopy. *Appl. Phys. Lett.* **2000**, *76*, 1419–1421.
- (23) Bond, T. C.; Bergstrom, R. W. Light Absorption by Carbonaceous Particles: An Investigative Review. *Aerosol Sci. Technol.* **2006**, *40*, 27–67.
- (24) Zangmeister, C. D.; Ma, X.; Zachariah, M. R. Restructuring of Graphene Oxide Sheets into Monodisperse Nanospheres. *Chem. Mater.* **2012**, *24*, 2554–2557.
- (25) Ma, X.; Zachariah, M. R. Size-Resolved Kinetics of Zn Nanocrystal Hydrolysis for Hydrogen Generation. *Int. J. Hydrogen Energy* **2010**, *35*, 2268–2277.
- (26) Ma, X.; Lall, A. A.; Mulholland, G. W.; Zachariah, M. R. Evaporation Anisotropy of Free Nanocrystals. *J. Phys. Chem. C* **2011**, *115*, 16941–16946.
- (27) Zhou, L.; Rai, A.; Piekielek, N.; Ma, X. F.; Zachariah, M. R. Ion-Mobility Spectrometry of Nickel Nanoparticle Oxidation Kinetics: Application to Energetic Materials. *J. Phys. Chem. C* **2008**, *112*, 16209–16218.
- (28) Ma, X. F.; Zachariah, M. R. Oxidation Anisotropy and Size-Dependent Reaction Kinetics of Zinc Nanocrystals. *J. Phys. Chem. C* **2009**, *113*, 14644–14650.
- (29) Lall, A. A.; Ma, X.; Guha, S.; Mulholland, G. W.; Zachariah, M. R. Online Nanoparticle Mass Measurement by Combined Aerosol Particle Mass Analyzer and Differential Mobility Analyzer: Comparison of Theory and Measurements. *Aerosol Sci. Technol.* **2009**, *43*, 1075–1083.
- (30) Gillis, K. A.; Havey, D. K.; Hodges, J. T. Standard Photoacoustic Spectrometer: Model and Validation Using O₂ A-Band Spectra. *Rev. Sci. Instrum.* **2010**, *81*, 064902.
- (31) Havey, D. K.; Bueno, P. A.; Gillis, K. A.; Hodges, J. T.; Mulholland, G. W.; van Zee, R. D.; Zachariah, M. R. Photoacoustic Spectrometer with a Calculable Cell Constant for Measurements of Gases and Aerosols. *Anal. Chem.* **2010**, *82*, 7935–7942.
- (32) Becerril, H. A.; Mao, J.; Liu, Z.; Stoltenberg, R. M.; Bao, Z.; Chen, Y. Evaluation of Solution-Processed Reduced Graphene Oxide Films As Transparent Conductors. *ACS Nano* **2008**, *2*, 463–470.
- (33) Gao, W.; Alemany, L. B.; Ci, L.; Ajayan, P. M. New Insights into the Structure and Reduction of Graphite Oxide. *Nat. Chem.* **2009**, *1*, 403–408.
- (34) Li, J. L.; Kudin, K. N.; McAllister, M. J.; Prud'homme, R. K.; Aksay, I. A.; Car, R. Oxygen-Driven Unzipping of Graphitic Materials. *Phys. Rev. Lett.* **2006**, *96*, 176101.
- (35) Ma, L.; Wang, J. L.; Ding, F. Strain-Induced Orientation-Selective Cutting of Graphene into Graphene Nanoribbons on Oxidation. *Angew. Chem., Int. Ed.* **2012**, *51*, 1161–1164.
- (36) Fujii, S.; Enoki, T. Cutting of Oxidized Graphene into Nanosized Pieces. *J. Am. Chem. Soc.* **2010**, *132*, 10034–10041.
- (37) Kosynkin, D. V.; Higginbotham, A. L.; Sinitskii, A.; Lomeda, J. R.; Dimiev, A.; Price, B. K.; Tour, J. M. Longitudinal Unzipping of Carbon Nanotubes to Form Graphene Nanoribbons. *Nature* **2009**, *458*, 872.
- (38) Sun, T.; Fabris, S. Mechanisms for Oxidative Unzipping and Cutting of Graphene. *Nano Lett.* **2012**, *12*, 17–21.
- (39) Radovic, L. R.; Silva-Tapia, A. B.; Vallejos-Burgos, F. Oxygen Migration on the Graphene Surface. 1. Origin of Epoxide Groups. *Carbon* **2011**, *49*, 4218–4225.
- (40) Radovic, L. R.; Suarez, A.; Vallejos-Burgos, F.; Sofu, J. O. Oxygen Migration on the Graphene Surface. 2. Thermochemistry of Basal-Plane Diffusion (Hopping). *Carbon* **2011**, *49*, 4226–4238.
- (41) Li, Z. Y.; Zhang, W. H.; Luo, Y.; Yang, J. L.; Hou, J. G. How Graphene Is Cut upon Oxidation? *J. Am. Chem. Soc.* **2009**, *131*, 6320–6321.
- (42) Khawam, A.; Flanagan, D. R. Solid-State Kinetic Models: Basics and Mathematical Fundamentals. *J. Phys. Chem. B* **2006**, *110*, 17315–17328.
- (43) Jung, I.; Field, D. A.; Clark, N. J.; Zhu, Y.; Yang, D.; Piner, R. D.; Stankovich, S.; Dikin, D. A.; Geisler, H.; Ventrice, C. A., Jr.; Ruoff, R. S. Reduction Kinetics of Graphene Oxide Determined by Electrical Transport Measurements and Temperature Programmed Desorption. *J. Phys. Chem. C* **2009**, *113*, 18480–18486.
- (44) Barroso-Bujans, F.; Alegria, A.; Colmenero, J. Kinetic Study of the Graphite Oxide Reduction: Combined Structural and Gravimetric Experiments under Isothermal and Nonisothermal Conditions. *J. Phys. Chem. C* **2010**, *114*, 21645–21651.
- (45) Dreyer, D. R.; Park, S.; Bielawski, C. W.; Ruoff, R. S. The Chemistry of Graphene Oxide. *Chem. Soc. Rev.* **2010**, *39*, 228–240.
- (46) Wang, G. X.; Wang, B.; Park, J.; Yang, J.; Shen, X. P.; Yao, J. Synthesis of Enhanced Hydrophilic and Hydrophobic Graphene Oxide Nanosheets by a Solvothermal Method. *Carbon* **2009**, *47*, 68–72.
- (47) Kaniyoor, A.; Ramaprabhu, S. A Raman Spectroscopic Investigation of Graphite Oxide Derived Graphene. *AIP Adv.* **2012**, *2*, 032183.
- (48) Saner, B.; Okyay, F.; Yurum, Y. Utilization of Multiple Graphene Layers in Fuel Cells. 1. An Improved Technique for the Exfoliation of Graphene-Based Nanosheets from Graphite. *Fuel* **2010**, *89*, 1903–1910.
- (49) Zhu, Y. W.; Murali, S.; Stoller, M. D.; Velamakanni, A.; Piner, R. D.; Ruoff, R. S. Microwave Assisted Exfoliation and Reduction of Graphite Oxide for Ultracapacitors. *Carbon* **2010**, *48*, 2118–2122.